The use of an unmanned aerial vehicle for fracture mapping within a marble quarry (Carrara, Italy): photogrammetry and discrete fracture network modelling

Riccardo Salvini*[1], Giovanni Mastrorocco[1], Marcello Seddaiu[1], Damiano Rossi[1], Claudio Vanneschi[1]

[1] University of Siena, Department of Environment, Earth and Physical Sciences and Centre of GeoTechnologies CGT, Via Vetri Vecchi 34, 52027, San Giovanni Valdarno, AR, Italy.

* Corresponding author. e-mail: riccardo.salvini@unisi.it

Abstract

This paper describes the use of a drone in collecting data for mapping discontinuities within a marble quarry. A topographic survey was carried out in order to guarantee high spatial accuracy in the exterior orientation of images. Photos were taken close to the slopes and at different angles, depending on the orientation of the quarry walls. This approach was used to overcome the problem of shadow areas and to obtain detailed information on any feature desired. Dense 3D point clouds obtained through image processing were used to rebuild the quarry geometry. Discontinuities were then mapped deterministically in great detail. Joint attitude interpretation was not always possible due to the regular shape of the cut quarry walls; for every discontinuity set we therefore also mapped the uncertainty. This, together with additional fracture characteristics, was used to build 3D discrete fracture network models. Preliminary results reveal the advantage of modern photogrammetric systems in producing detailed orthophotos; the latter allow accurate mapping in areas difficult to access (one of the main limitations of traditional techniques). The results highlight the benefits of integrating photogrammetric data with those collected through classical methods: the resulting knowledge of the site is crucially important in instability analyses involving numerical modelling.

1. Introduction

The Carrara district in Italy is one of the most productive marble quarrying regions in Europe and represents an important economic resource. Many people work in the quarries, and safety in the workplace is an overriding priority. In this context, the use of new technologies such as Unmanned Aerial Vehicle (UAV) systems to study and monitor mining and quarrying areas can be very important in risk assessment and management. Over the last decade, geomatic techniques such as Terrestrial Laser Scanning (TLS) and Digital Terrestrial Photogrammetry (DTP) have been used increasingly to characterise rock masses throughout the world (Abellán et al. 2006; Coggan et al. 2007; Ghirotti & Genevois 2007; Ferrero et al. 2009; Lato et al. 2009; Sturzenegger & Stead 2009a and b; Salvini et al. 2011; Jaboyedoff et al. 2012; Salvini et al. 2013; Francioni et al. 2015). One of the most common problems encountered in the use of these techniques, especially in the case of slopes with complex geometries, is the presence of occlusions. This study demonstrates how the use of UAV systems can overcome such limitations by acquiring data at different angles, depending on the orientation of walls. Photographs taken by UAV can be used to map all visible

discontinuities irrespective of their position, attitude or elevation from the ground. Quarry walls in the Carrara marble district can be up to hundreds of metres high and are dominated by natural slopes with very complex morphologies. In these quarries conventional structural and engineering geological survey data can be collected only at the foot of slopes or by climbing on high rock walls; these data often provide an incomplete understanding of the area.

The use of UAV can significantly improve the collection of geometric and structural data in such areas. The latest drone hardware and software developments allow their application in several fields of science, including the study of landslides and rockfall instability (Rau et al. 2011; Niethammer et al. 2012; Danzi et al. 2013; Salvini et al. 2014; Giordan et al. 2015; Francioni et al. 2015; Turner et al. 2015). Digital Surface Models (DSMs), orthophotos and 3D models derived from processed UAV images allow accurate mapping of joint geometries and their degree of uncertainty. Such data can then be used both for the calculation of yield (in terms of commercial value) and for the deterministic analysis of stability and the study of stress distribution within slopes (in terms of safety). For these purposes, a case study was completed in the Lorano open pit (Apuan Alps, Italy). In particular, data from a UAV photogrammetric survey was used to map fractures in a buttress-shaped remnant of previous excavation activities. Data were integrated with information from traditional engineering geological surveys to derive important parameters such as fracture orientation, intensity, density, size and termination. This enabled the creation of a 3D Discrete Fracture Network (DFN) model built on the basis of geomechanical data from traditional field surveys, the literature, laboratory tests, UAV image processing and geological photointerpretation. The DFN approach allows for an excellent use of collected fracture data and can be used to obtain a 2D or 3D Synthetic Rock Mass (SRM) model. DFN is a stochastic representation of discontinuities derived from the analysis of fracture density and intensity parameters that are generally obtained by mapping line traces (discontinuities) on two- or three-dimensional rock exposures. The fracture pattern, which takes into account the natural variability of the rock mass, is therefore based on statistical inputs. The various stochastic models are expected to differ; consequently, several models are required to understand simulation outcomes (Weir & Fowler 2014).

The DFN approach is quite new in the field of engineering geology. Before 2010 there was almost no mention of DFNs in the proceedings of major conferences on rock mass stability analysis (Lorig 2014). However, in recent years the DFN approach has gained increased usage in numerical modelling for rock engineering purposes (Bakun-Mazor et al. 2009; Scholtès & Donzé 2012; Bahrani et al. 2014; Grenon et al. 2014; Lei et al. 2014; Borghi et al. 2015). This is because the method overcomes one of the principal limitations of traditional analyses: the unrealistic assumption of ubiquitous joints of infinite length (Weir & Fowler 2014). Ideally, each joint in the rock mass should be characterised; however, the limited visibility of discontinuities (outcrop observation) precludes such detailed study (Dershowitz & Einstein 1988), even using the most recent geomatic and geophysical techniques. DFN modelling is therefore the best available option. In this work, the DFN model was built to maximise the use of fracture data collected through exposure mapping and to build an SRM model. Since the accuracy of the DFN model depends directly on the quality and quantity of available data, high-definition images and 3D information derived from UAV data can make a strong

contribution. In addition, both certain and uncertain joint attitudes were discerned in this work. This was done because on a flat surface like a quarry wall face it is difficult to correctly interpret the set to which a discontinuity belongs, an important point requiring further studies in the context of DFN model calibration and validation.

2. Geographic and geological setting

The Lorano open pit is located in the Province of Massa and Carrara, northwestern Tuscany (Italy). In 1997 a rockfall in the quarry interrupted excavation activities for a few weeks. Remediation works were subsequently carried out with the aim of ensuring safety, and a marble buttress accessible from three sides was emplaced (figure 1). Due to the ongoing quarrying activity the buttress is now about 150 m high, 30 m wide and 40 m thick.

The quarry is located in a fold-and-thrust belt of the Northern Apennines, which formed through the Tertiary collision (66 Ma) between the Sardinia-Corsica block and the Adria plate (Boccaletti et al. 1971; Scandone 1979; Dercourt et al. 1986). The study area belongs to the Apuan Alps metamorphic complex (figure 2), first described by Zaccagna (1932); deep levels of the belt are exposed in this, the largest tectonic window in the inner Northern Apennines (Elter 1975; Carmignani & Kligfield, 1990; Molli, 2008). The metamorphic complex consists of two main tectono-metamorphic units, the "Apuan unit" and the overlying "Massa unit". According to the classical interpretation, the regional tectonic setting of the Apuan Alps is the result of two main tectono-metamorphic events, D1 and D2 (Carmignani & Kligfield, 1990). D1, the ductile compressional event, was determined by the Tertiary continental collision between the Sardinia-Corsica block and the Adria plate; it was followed by the D2 extensional event that led to isostatic re-equilibration (Carmignani & Kligfield, 1990). During the D1 event, tectonic units of the Tuscan and Ligurian domains were stacked, and deformation occurred progressively in two stages (Molli & Meccheri, 2000). The greenschist foliation (Sp) in the axial plane of isoclinal micro- to kilometre-scale folds represents the main stage. During the D2 event, the previously formed structures were deformed and developed different generations of folds and local high-strain zones associated with exhumation and vertical shearing (Molli 2012). The late stages of D2 are characterised by the development of brittle structures (low- and high-angle faults and joint systems) associated with the final exhumation and uplift of the metamorphic units in the context of the late to post-orogenic regional extension of the inner Northern Apennines (Molli et al., 2010).

Figure 1: Study area. Topography of the site (in the centre, from Salvini et al., 2014); black circle indicates the marble buttress; inset map shows the location of the study area. Panoramic view of the quarry, with the investigated buttress highlighted by a rectangle (upper left); southern side of the buttress (upper right), western side of the buttress (lower left) and eastern side of the buttress (lower right).

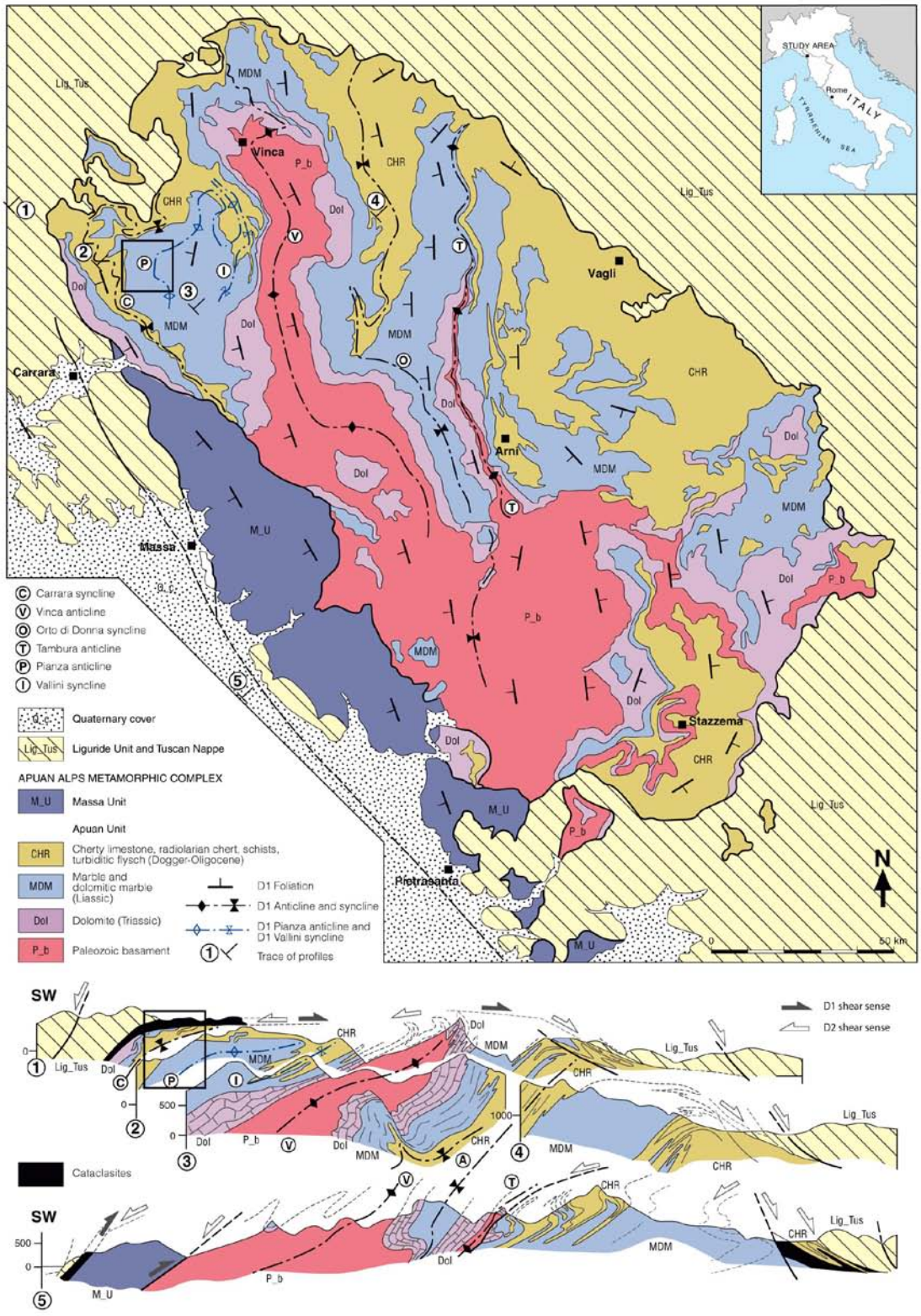

Figure 2: Geological sketch map of the Apuan Alps. The black rectangle indicates the location of the quarry (from Salvini et al. 2015).

According to Carmignani et al. (2002), the brittle stages of the D2 phase led to the development of the three main discontinuity systems that characterise the marble district. The first system (J1), shows an average anti-Apennine direction ranging from N20-30°E to N80-90°E and a general vertical or subvertical inclination (dipping up to 50-60° both to the NW and the SE). The second system (J2) ranges in direction from N120°E to N150°E with a medium-high dip generally to the E and the NE. The third and last system (J3) is often pervasive and almost parallel to the foliation (Sp); it shows a direction similar to J2 and dips steeply to the SW.

The Lorano marble quarry is located in the normal limb of the “Pianza anticline” which, together with the “Vallini syncline”, represents a coupled antiform-synform with a core of Jurassic marbles and cherty meta-limestone. These are minor folds (hectometre-scale) between two D1 structures known as the “Carrara syncline” and “Vinca anticline” located to the NW and the SE, respectively (Molli & Meccheri 2012). Most of the quarried marble belongs to the White Marble Group, characterised by homogeneous marbles of medium-fine grain size (about 100-200 μm), and Ordinary Marble (Meccheri 1996), with a medium grain size (about 200 μm). Two subordinate types of marble in the quarry are Veined Grey Marble and Breached Marble (Carmignani et al. 2007).

3. Engineering geological survey

An engineering geological survey was carried out to characterise the geomechanical properties of discontinuities. Data were collected in accessible areas using traditional scan-line mapping techniques whereby all the discontinuities that intersect a defined scan line are recorded. About 100 discontinuities longer than 10 m were identified in seven scan lines. Collected data were compared with those of Profeti and Cella (2010) for the same area and integrated with DTP and TLS data from inaccessible zones, as described in Francioni et al. (2015). The attitude of 301 joints was calculated from TLS and an additional 236 discontinuities were manually measured from the photointerpretation of UAV imagery (Francioni et al. 2015). Data processing revealed the following four sets of discontinuities (named K1, K2, K3 and S1 in accordance with Profeti and Cella, 2010) describing the current state of the buttress (figure 3): S1 (foliation) - SW dipping with average dip of about 50°, corresponding to Sp of Carmignani et al. (2002); K1 - SE dipping, subvertical, corresponding to J1 of Carmignani et al. (2002); K2 - NE dipping with average dip of about 50°, corresponding to J2 of Carmignani et al. (2002); and K3 - SW dipping, subvertical, corresponding to J3 of Carmignani et al. (2002).

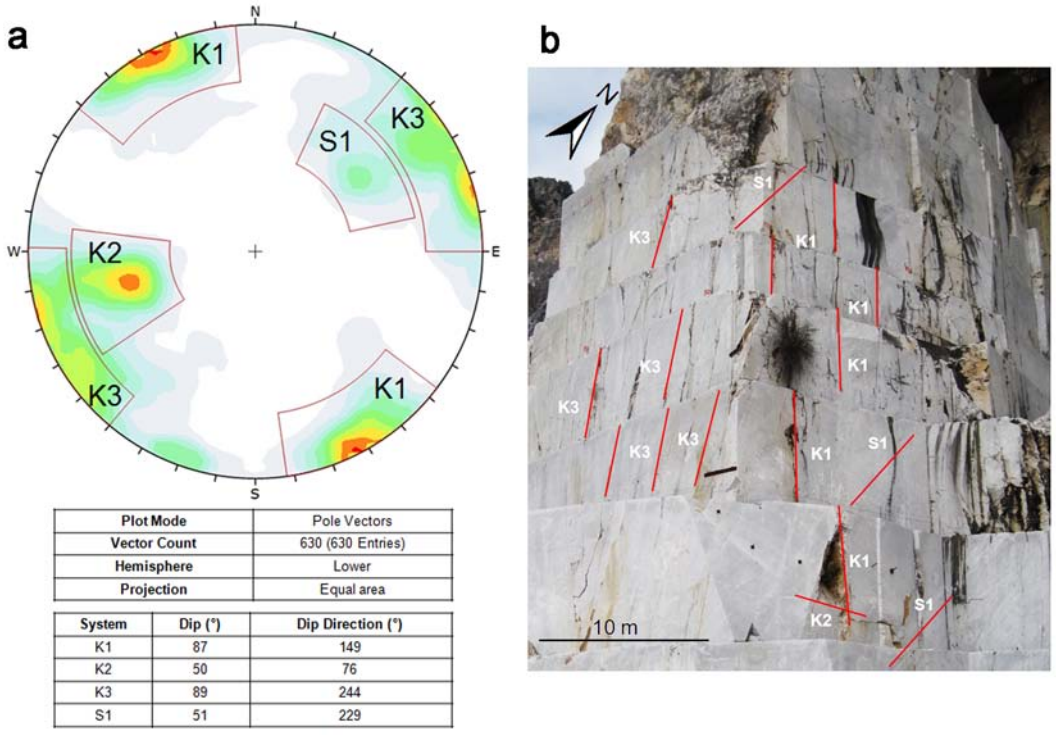

Plot Mode	Pole Vectors
Vector Count	630 (630 Entries)
Hemisphere	Lower
Projection	Equal area

System	Dip (°)	Dip Direction (°)
K1	87	149
K2	50	76
K3	89	244
S1	51	229

Figure 3: Joint systems. a) Pole plots and mean attitudes of joint systems from engineering geological, DTP and TLS surveys. Data are shown in stereographic projection using the Schmidt equal-area method. b) Examples of K1, K2, and K3 joint systems and S1 foliation in the buttress (from Salvini et al., 2015).

The K1, K2 and K3 systems are characterised by metre spacing, millimetre to centimetre apertures, moderate roughness and no infill. According to the Rock Mass Rating (RMR - Bieniawski, 1989) the rock mass is of good quality (basic RMR or RMRb = 76). Geological Strength Index (GSI - Hoek & Brown 1997) values within engineered areas (i.e. open pit) are variable and differ with respect to those of the natural rock outcrops (i.e. the slope above). Considering the characteristics of the marble, the GSI was estimated to vary between 50 and 60 on the natural slope and between 70 and 80 on the face of the open pit. This variation is probably due to the degree of weathering of the natural slope surface and to the fact that the joint spacing usually increases with depth (Francioni et al. 2015).

4. UAV survey

Due to the considerable height of the marble buttress, a photogrammetric survey was carried out using UAV technology to obtain high-resolution digital products (DSMs and orthophotos). Given the morphology of the area, a multi-rotor Falcon 8 UAV vehicle (Asctec^{TM} Gmbh) equipped with a Sony^{TM} NEX-5N digital camera was used (Table 1). Falcon 8 consists of eight electric rotors, a remote control system (mobile ground station) and software for flight plan management. The UAV is equipped with a GPS and an Inertial Navigation System (INS) that can record 3D spatial coordinates and the orientation of the camera at every shot (detailed description of the on board systems are reported in table 2).

Table 1. UAV and camera specifications.

UAV Type	Dimensions	Engines	Rotor diameter	Empty weight	Max. take off weight
V-Form Octocopter	770 x 820 x 125 mm	Brushless motors	8" (~ 20 cm)	1.1 kg	2.3 kg
Camera	**Sensor type**	**Sensor Size (mm)**	**Image size (pixel)**	**Pixel size (mm)**	**Focal length (mm)**
Sony NEX-5	CMOS	23.4 x 15.6	4592 x 3056	0.004763	16.0121

Table 2. UAV on board system specifications.

Device	Model	Main features
GPS	u-blox LEA-6	GPS L1 frequency, C/A Code Velocity accuracy of 0.1 m/s Heading accuracy of 0.5°
Gyroscope	Analog Devices - ADXRS610	Measurement range ± 300°/s Sensitivity of 6 mV/°/s
Accelerometer	Memsic - MXR9500G/M	Tri-axis sensor Measurement range ± 1.5 g Sensitivity of 500 mV/g
Compass	Honeywell - HMC5843	Tri-axis magnetoresistive sensor Field range ± 4 gauss Cross-Axis sensitivity of ±0.2 %FS/gauss
Barometer	Freescale - MPXA6115A	Pressure range 15 - 115 kPa Accuracy of ±1.5% V_{FSS} (0° to 85°C) Sensitivity of 45.9 mV/kPa

Five vertical flights with 80% overlap and 40% sidelap ensured coverage of the entire area; the photos were taken from an average distance of 30 meters from the slope surface (Figure 4), yielding an estimated Ground Sample Distance (GSD) of about 1 cm.

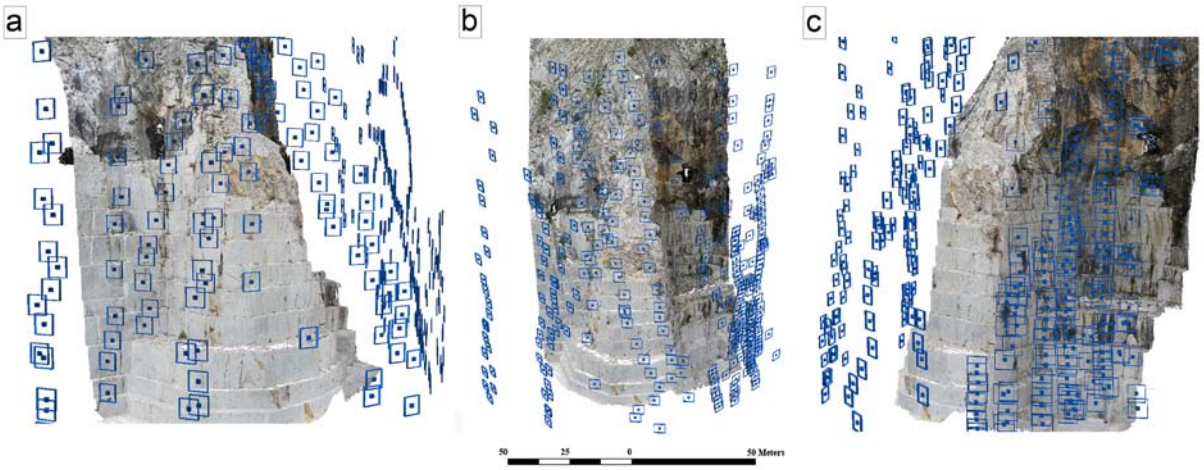

Figure 4. Panoramic views of the camera positions. a) west side of the buttress; b) south side of the buttress; c) east side of the buttress.

With the aim of improving the external orientation and level of accuracy of the entire photogrammetric model, a topographic survey was carried out using a Leica™ TCRP 1203 + R1000 reflectorless Total Station (TS) and two geodetic Leica™ 1200 GPS receivers. Due to the complex morphology of the buttress and the large area, a large number of Ground Control Points (GCPs) were used to orient the photogrammetric model. The Total Station was used to acquire 54 evenly spaced GCPs within the marble buttress. Two geodetic devices operating in static mode were used to obtain the geographic coordinates of two points: the origin of the survey and its zero-Azimuth direction. The GPS data acquired were corrected using contemporary data recorded by two permanent GPS stations located in Lucca and Borgo a Mozzano (Francioni et al. 2015).

Specific post-processing was used to determine the absolutes coordinates of all GCPs. The 391 photos acquired through the UAV survey were processed using the Agisoft™ PhotoScan Professional software, version 1.2.3 (Agisofte, 2016). This software, based on specific feature extraction algorithms, was used to solve the camera's interior and external orientation parameters and extract georeferenced products such as 3D point clouds, DSMs, orthophotos and textured models. The first task carried out in PhotoScan was alignment processing. This was used to solve the interior and relative orientation parameters and to extract millions of Tie Points. Although the software allows for a Tie Point extraction limit, this parameter was set to 0 (no limit) in order to improve alignment and obtain a lower reprojection error. At the end of the process PhotoScan was able to align all the images and extract more than 2 million Tie Points with an average reprojection error of about 0.2 pixels.

Twenty-nine GCPs measured with the TS during the topographic survey were used as control points for georeferencing the model and solving the exterior (absolute) orientation parameters. The remaining 25 GCPs were used as Check Points to assess the accuracy of the photogrammetric model. This operation was carried out by identifying the features measured through the topographic survey directly on the photos. Each feature was also associated with its relative 3D geographic coordinates.

PhotoScan's *optimize* tool (Agisoft, 2016) was used to adjust the estimated camera positions and to remove possible non-linear deformations, minimizing the errors due to reprojection and misalignment of the photos. At the end of the process the estimated Root Mean Square Error (RMSE) of GCPs was 0.029 metres, and that of the Check Points was 0.033 metres.

In order to assess the reliability of the obtained RMSEs, the selection and number of Control and Check Points on the buttress were varied. Table 3 shows the results of three tests completed by varying the number of Control and Check Points. Considering 54 GCPs, when the number of Control and Check Points is varied from 29 to 16 and from 25 to 38 respectively, the resulting RMSE does not change (only 1 mm for Check Points). In order to validate the RMSE achieved with 29 Control Points, the accuracy of 10 Check Points was determined: 0.025 m (Table 3). From this it follows that the availability of a large number of spatially well distributed GCPs allows accuracy assessment thanks to the numerous Check Points and the correct orientation of images. Figure 5 shows the spatial distribution and error of GCPs in the final configuration (29 Control Points and 25 Check Points).

Table 3. Number of GCPs used for the orientation of images and the resulting RMSE.

Test	Nr. Control Points	RMSE Control Points (m)	Nr. Check Points	RMSE Check Points (m)
1	29	0.029	25	0.033
2	16	0.029	38	0.034
3	29	0.027	10	0.025

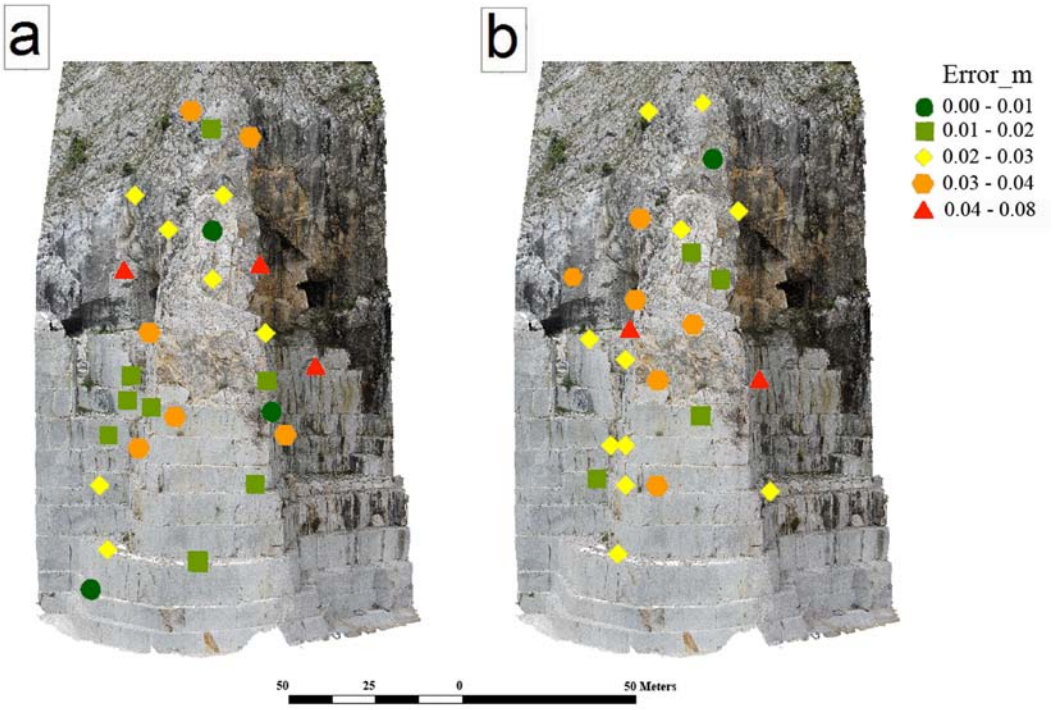

Figure 5. Spatial distribution and error of a) Control Points and b) Check Points.

Once the resulting RMSEs were checked and accepted, a dense cloud consisting of more than twenty million points was created (using the settings *Medium* quality and *Aggressive* depth filtering). This dense cloud was used to create a mesh of about 4 million facets. Lastly, the 3D model was used to create the orthophotos of the buttress by removing image distortion due to camera characteristics (i.e. lens distortions), camera tilt, and topographic relief displacement. Unlike an uncorrected aerial photograph with a perspective projection, an orthophoto is geometrically corrected ("orthorectified") and can be used to measure true distances since it is "scale-corrected". Four different planes of reference, one for each side of the buttress (eastern, southern and western) and an overhead view, were selected for measurements. The resulting orthophotos with a spatial resolution of 1 cm/pixel were exported in the local coordinate system; only the top view was projected into the Italian-National Gauss-Boaga system (Figure 6).

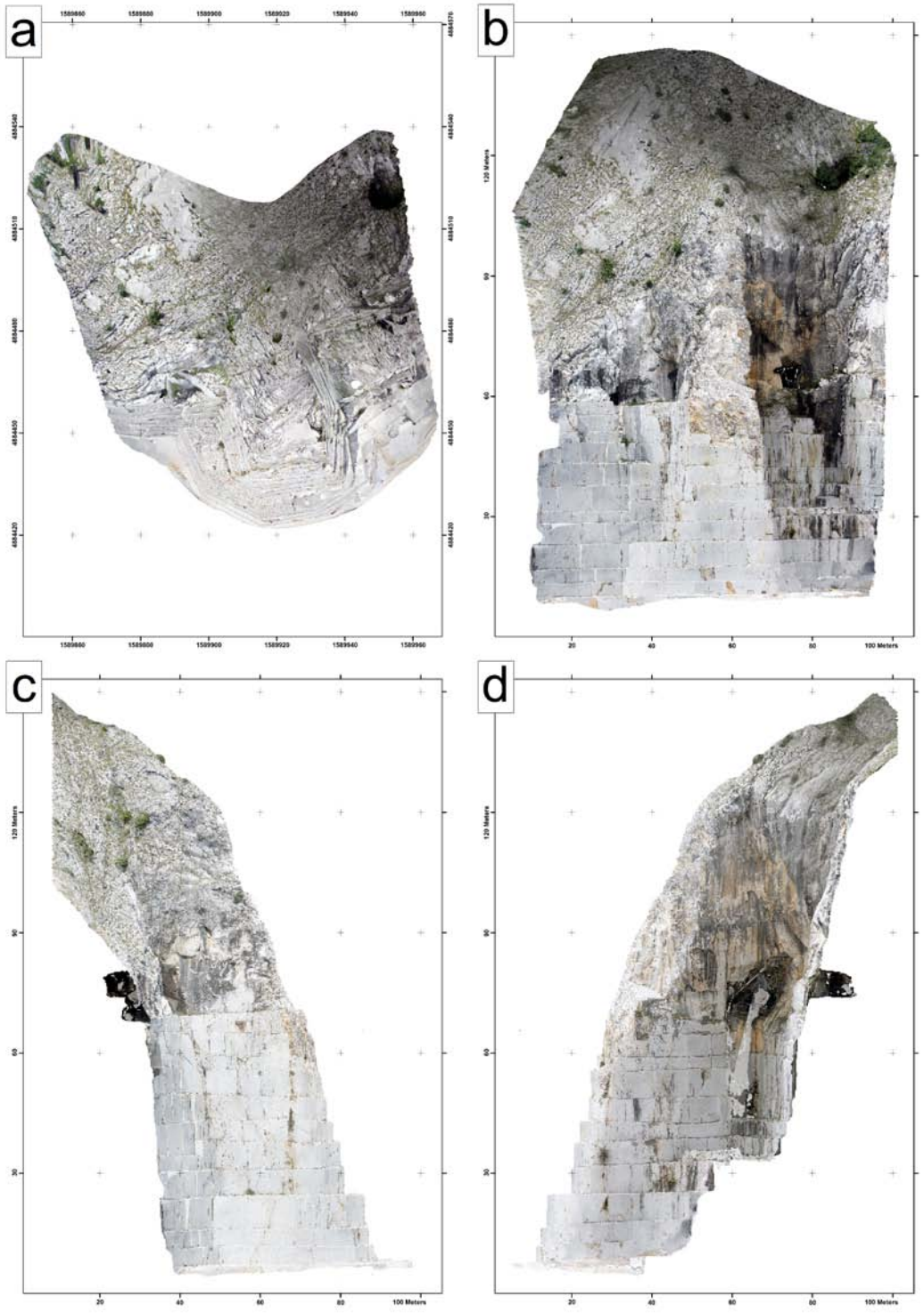

Figure 6. Orthophotos. a) top view of the buttress, b) south side of the buttress, c) west side of the buttress, d) east side of the buttress.

5. Fracture mapping and DFN modelling

Different software allows DFN model simulations by defining the statistical distribution of joint length and intensity. In this case study the FracSim3D software (Xu & Dowd 2010) was used to create the 3D DFN model. This software can simulate 2D and 3D stochastic rock fracture networks using marked point processes. The geometric characteristics supported by this software are fracture location, size (diameter) and orientation. These properties can be defined using different processes and distribution functions (Table 4).

Table 4. Distribution functions available in FracSim3D.

Geometrical process and distribution functions		
Locations process	**Size distribution**	**Orientation distribution**
Homogeneous (Poisson) model	Uniform	Uniform
Non-homogeneous process	Exponential	Wrapped normal (2D)
Cluster process	Lognormal	Von Moses (2D)
Cox process		Fisher

In this case the homogeneous model was adopted for fracture locations, whereas exponential and Fisher distributions were used for the size and orientation of the discontinuities respectively. The first step is to simulate the fracture location by generating a number of points. For any set, the number of points falling inside a certain area (A), N(A), follows a Poisson distribution with mean $\gamma * v(A)$, where v(A) is the volumetric measure of A and γ is the intensity of the distribution. The second step is to simulate the geometry of each individual fracture. A stochastic network of discontinuities can be generated in this way.

The "P" system, introduced by Dershowitz and Herda (1992), was adopted in this case study to define discontinuity density (P_{10} and P_{20}) and intensity (P_{21}). It is a common method for defining fracture density/intensity parameters starting from line traces mapping on two-dimensional survey windows, and one that provides a convenient framework for moving between differing scales and dimensions. The mentioned parameters can be calculated as follows:

P_{10} (m^{-1}) = (number of fractures / length of scan line)

P_{20} (m^{-2}) = (number of fractures / area of exposure)

P_{21} (m/m^2) = (length of fracture traces / area of exposure)

The method was chosen for its simplicity and for the availability of high spatial resolution orthophotos and 3D information on the buttress. Three high-resolution orthophotos (eastern, southern and western sides of the buttress) were used to derive the "P" system parameters. In particular, a detailed cartographic approach within a Geographic Information System (GIS) was adopted. Six different surface mapping windows, two for each side of the marble buttress, were drawn on the orthophotos using the ESRI™ ArcMap software. The survey windows, each measuring 10 m x 15 m, were spaced a few metres apart in the central parts of the buttress. All discontinuities

observed within the windows were then measured in order to calculate the P_{10}, P_{20} and P_{30} values. In this case the flatness of the quarry wall face represented in a 2D orthophoto complicates things because it makes it difficult to assign a discontinuity to the correct set identified through the engineering geological and geomatic surveys (only line traces are visible). The apparent inclination of every discontinuity set on each side of the buttress was therefore calculated.

Because the buttress faces are irregular due to quarrying, the difficulties relating to fracture characterization partially persisted. With the aim of facilitating this operation, the top view orthophoto was used to observe the quarry benches from above (so as to "see" a second orthogonal surface). The 3D model formed by the mesh built in PhotoScan from the dense cloud and the orthophotos of the buttress were used within the ESRI™ ArcGIS Pro software to have an additional control of joint attitude in 3D visualization. No additional fractures were mapped in the 3D view since the rock fracture network was simulated using a stochastic, not a deterministic approach.

By combining 2D and 3D views with data collected during in-situ surveys, discontinuities on all three sides of the marble buttress were identified with a high degree of certainty. Despite efforts to minimize uncertainty, discontinuities with uncertain attitude were also mapped because some highly dipping sets (e.g. K1 and K3) produce similar line traces on the buttress surface. The deterministic maps of discontinuities (with length greater than 2 m) are shown in figures 7 and 8.

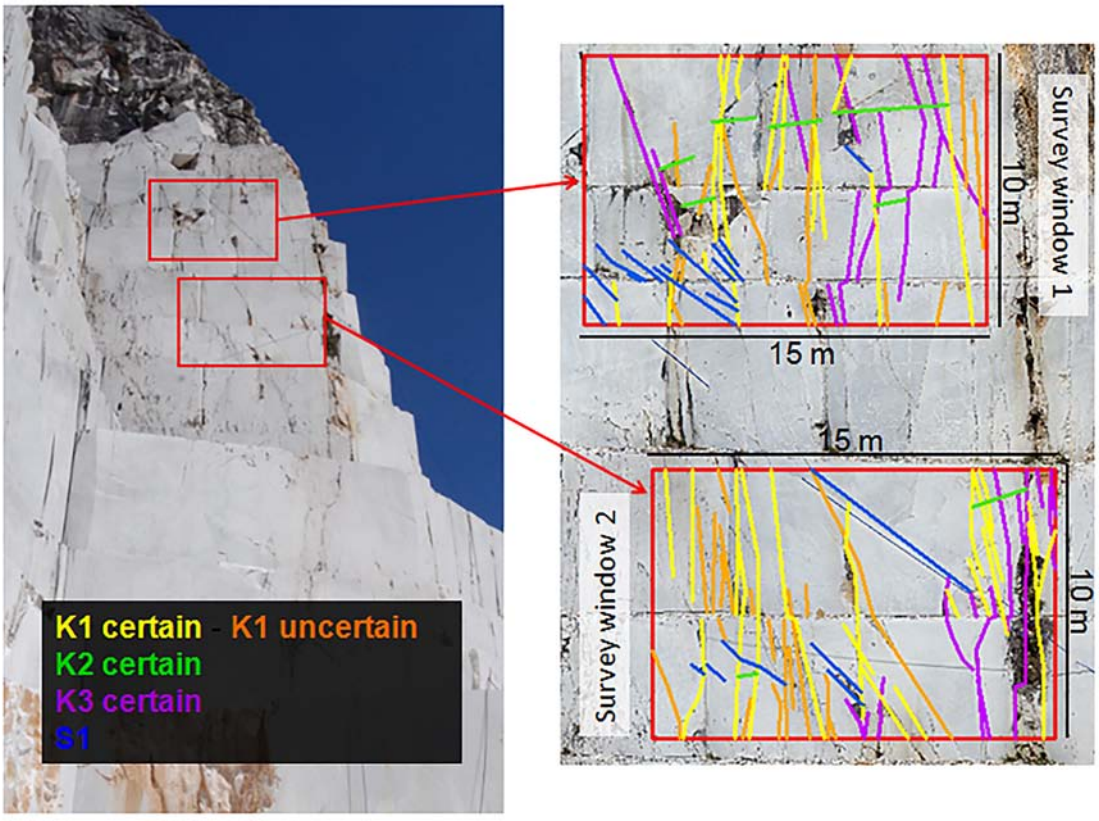

Figure 7. Survey windows 1 and 2 used to map discontinuity sets K1, K2 and K3, as well as foliation S1, on the western side of the buttress.

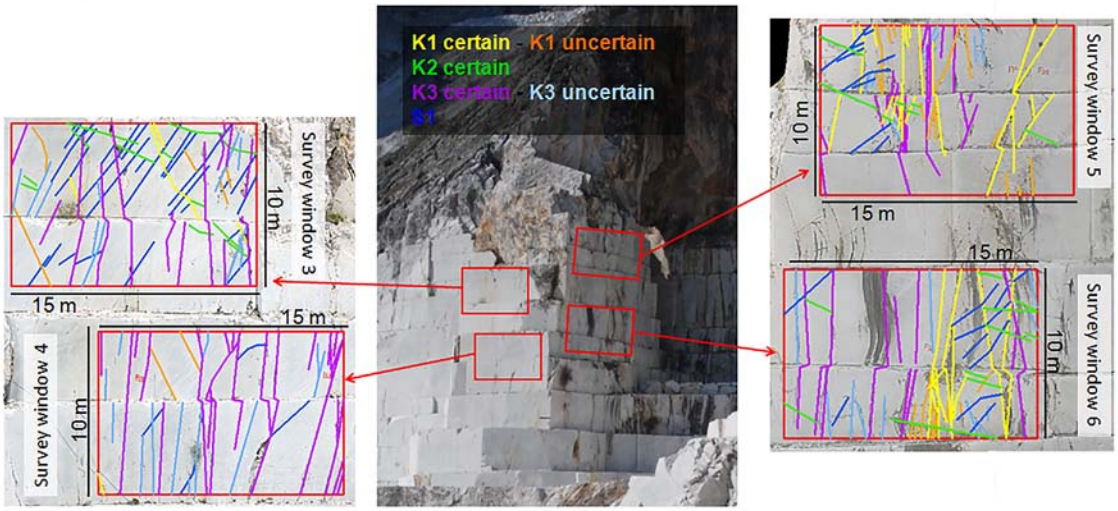

Figure 8. Survey windows 3 to 6 used to map discontinuity sets K1, K2 and K3, as well as foliation S1, on the southern and eastern sides of the buttress.

After identifying discontinuities and using the P system, it was possible to measure and collect all data required to produce several 3D DFN models using the FracSim3D code. In this context, P_{10}, P_{20} and P_{21} values were calculated using the six windows located on all three sides of the buttress. In particular, P values were calculated for both the certain ($P_{certain}$, including only joints assigned with certainty to a specific joint set; see figures 7 and 8) and uncertain attitudes ($P_{certain+uncertain}$, including also those joints of uncertain attitude; see figures 7 and 8) of joint systems. Tables 5, 6 and 7 show the results in terms of the calculated P values.

Table 5. Calculated values of P_{10}, P_{20} and P_{21} in survey windows 1 and 2.

	Window 1			**Window 2**		
Set	**P_{10} (m^{-1})**	**P_{20} (m^{-2})**	**P_{21} (m/m^2)**	**P_{10} (m^{-1})**	**P_{20} (m^{-2})**	**P_{21} (m/m^2)**
$K1_{certain}$	0.400	0.93	0.383	0.600	0.133	0.625
$K1_{certain+uncertain}$	0.667	0.180	0.659	1.133	0.253	0.978
$K2_{certain}$	0.000	0.040	0.079	0.000	0.013	0.019
$K2_{certain+uncertain}$	0.000	0.040	0.079	0.000	0.013	0.019
$K3_{certain}$	0.333	0.067	0.381	0.333	0.087	0.285
$K3_{certain+uncertain}$	0.333	0.067	0.381	0.333	0.087	0.285
S1	0.000	0.087	0.146	0.000	0.040	0.108

346 Table 6. Calculated values of P_{10}, P_{20} and P_{21} in survey windows 3 and 4.

	WINDOW 3			WINDOW 4		
Set	**P_{10} (m^{-1})**	**P_{20} (m^{-2})**	**P_{21} (m/m^2)**	**P_{10} (m^{-1})**	**P_{20} (m^{-2})**	**P_{21} (m/m^2)**
$K1_{certain}$	0.133	0.027	0.080	0.000	0.007	0.009
$K1_{certain+uncertain}$	0.133	0.060	0.153	0.000	0.020	0.053
$K2_{certain}$	0.067	0.080	0.162	0.000	0.000	0.000
$K2_{certain+uncertain}$	0.067	0.080	0.162	0.000	0.000	0.000
$K3_{certain}$	0.333	0.100	0.445	0.733	0.153	0.728
$K3_{certain+uncertain}$	0.533	0.167	0.634	1.067	0.233	0.996
S1	0.467	0.180	0.493	0.133	0.027	0.065

347 Table 7. Calculated values of P_{10}, P_{20} and P_{21} in survey windows 5 and 6.

	WINDOW 5			WINDOW 6		
Set	**P_{10} (m^{-1})**	**P_{20} (m^{-2})**	**P_{21} (m/m^2)**	**P_{10} (m^{-1})**	**P_{20} (m^{-2})**	**P_{21} (m/m^2)**
$K1_{certain}$	0.733	0.127	0.412	0.333	0.067	0.407
$K1_{certain+uncertain}$	0.933	0.213	0.581	0.333	0.127	0.505
$K2_{certain}$	0.067	0.047	0.077	0.000	0.067	0.156
$K2_{certain+uncertain}$	0.067	0.047	0.077	0.000	0.067	0.156
$K3_{certain}$	0.533	0.100	0.309	0.467	0.067	0.430
$K3_{certain+uncertain}$	0.533	0.160	0.399	0.533	0.140	0.628
S1	0.000	0.060	0.116	0.133	0.067	0.184

348 In addition, information about standard deviations of the P values for every system are
349 exposed in table 8.

350 Table 8. Calculated SD for P_{10} values.

	SD P_{10}	**SD P_{20}**	**SD P_{21}**
K1	0.367	0.078	0.291
K2	0.034	0.03	0.067
K3	0.217	0.051	0.213

351 The values calculated on different survey windows show good correlation and, as
352 mentioned earlier, can be used to generate a number of DFN models by varying the
353 distribution functions that characterise the discontinuity sets. Figure 9 shows an
354 example of a DFN model generated using FracSim3D. In this case certain P_{10} values
355 obtained on windows 3 and 4 were used to define joint density, a Fisher distribution was
356 used for the orientation of discontinuities and an exponential distribution was used to
357 assess discontinuity lengths. The software can also be used to associate additional
358 geomechanical properties to the discontinuities using a uniform, normal, exponential,
359 lognormal or non-parametric distribution.

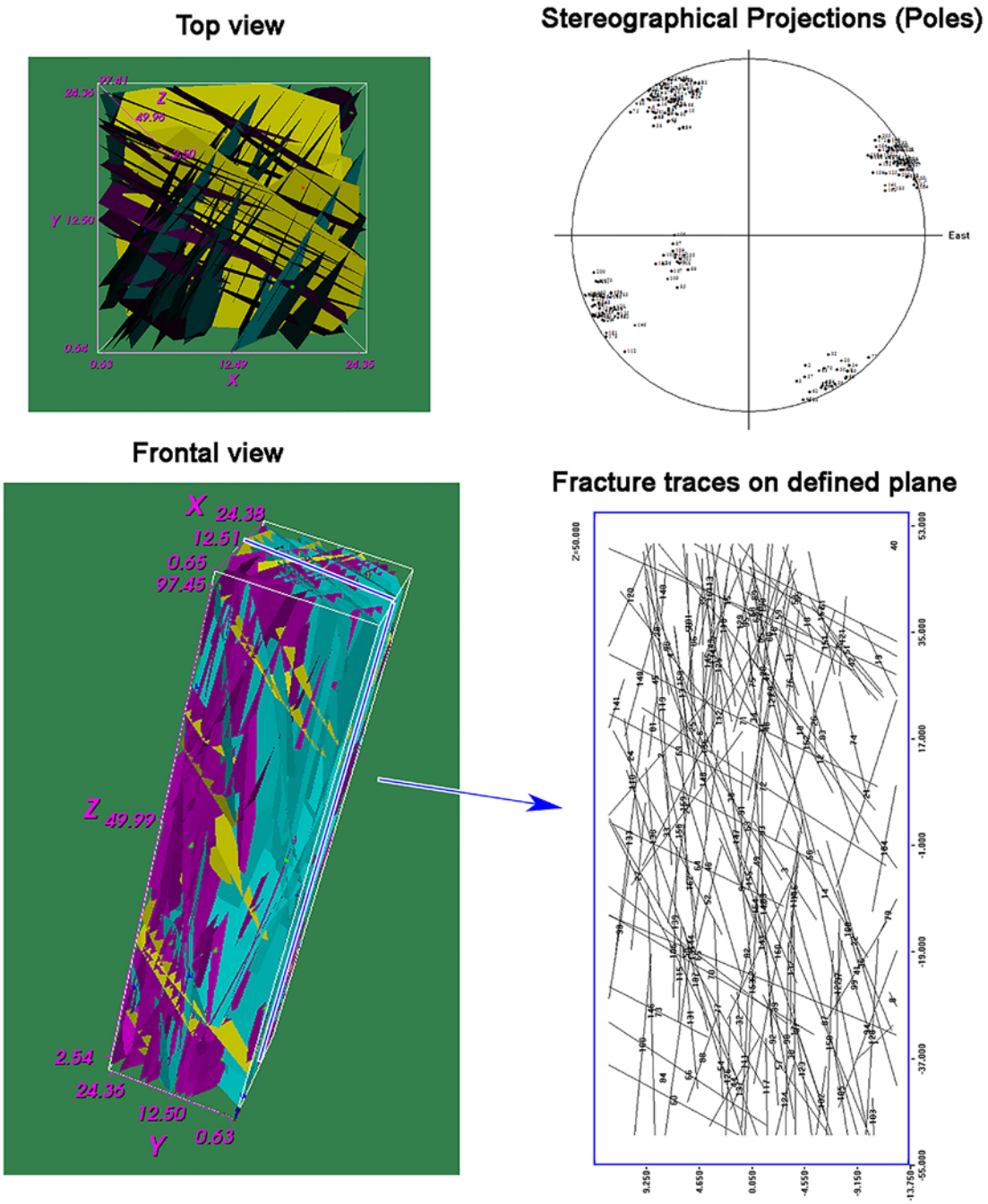

Figure 9. Generation of a DFN model for the marble buttress using FracSim3D. K1, K2 and K3 joint sets included.

The S1 foliation was not included in the shown model because it does not represent a real plane of discontinuity in the studied quarry. Nevertheless, it is a plane of weakness that could affect the stability of the buttress and will be the subject of future research.

Several models can be created to assess the influence of uncertainty on the SRM model and improve the reliability of results. This is particularly important because several trial runs can be completed and analysed in order to obtain reliable results for a stochastic representation of a natural discontinuity network. For example, figures 10 and 11 show

2D representations (including stereonets and normal probability plots for fracture lengths) of two DFN models generated using respectively certain and certain+uncertain P_{10} values (as average among all the 6 mapped windows).

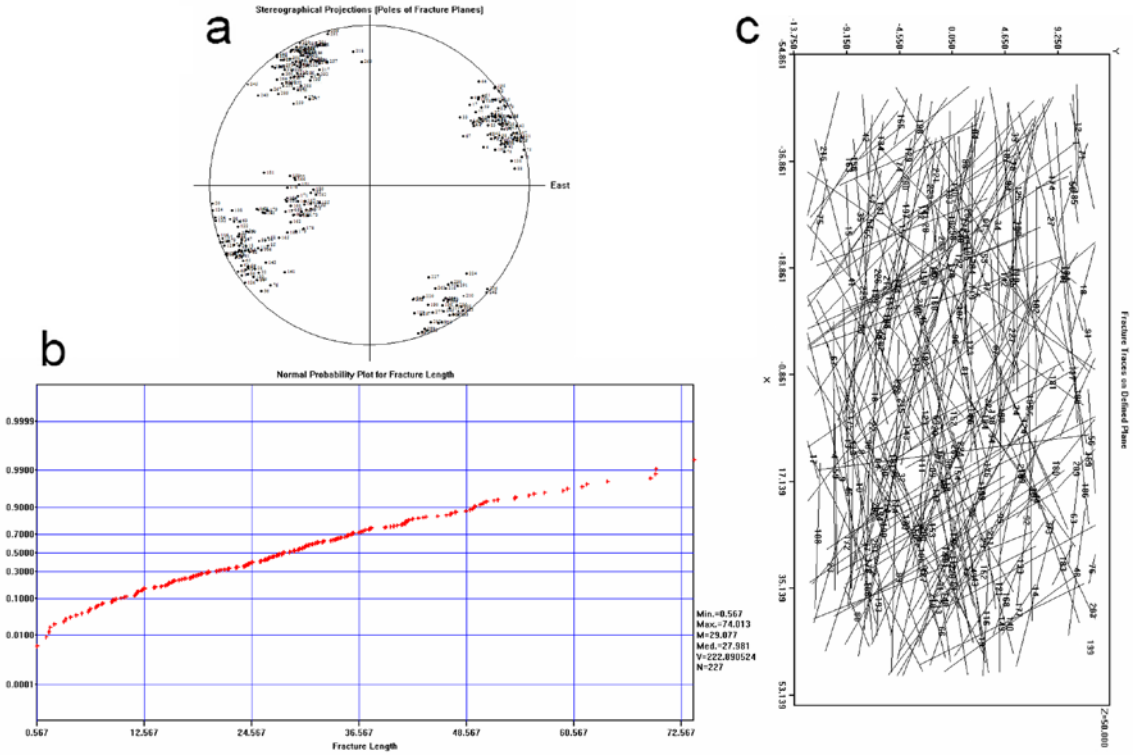

Figure 10. Generation of a DFN model for the marble buttress using FracSim3D with P_{10} certain values. K1, K2 and K3 joint sets included. a) Stereonet, b) Normal probability plot for fracture lengths, c) 2D DFN model section.

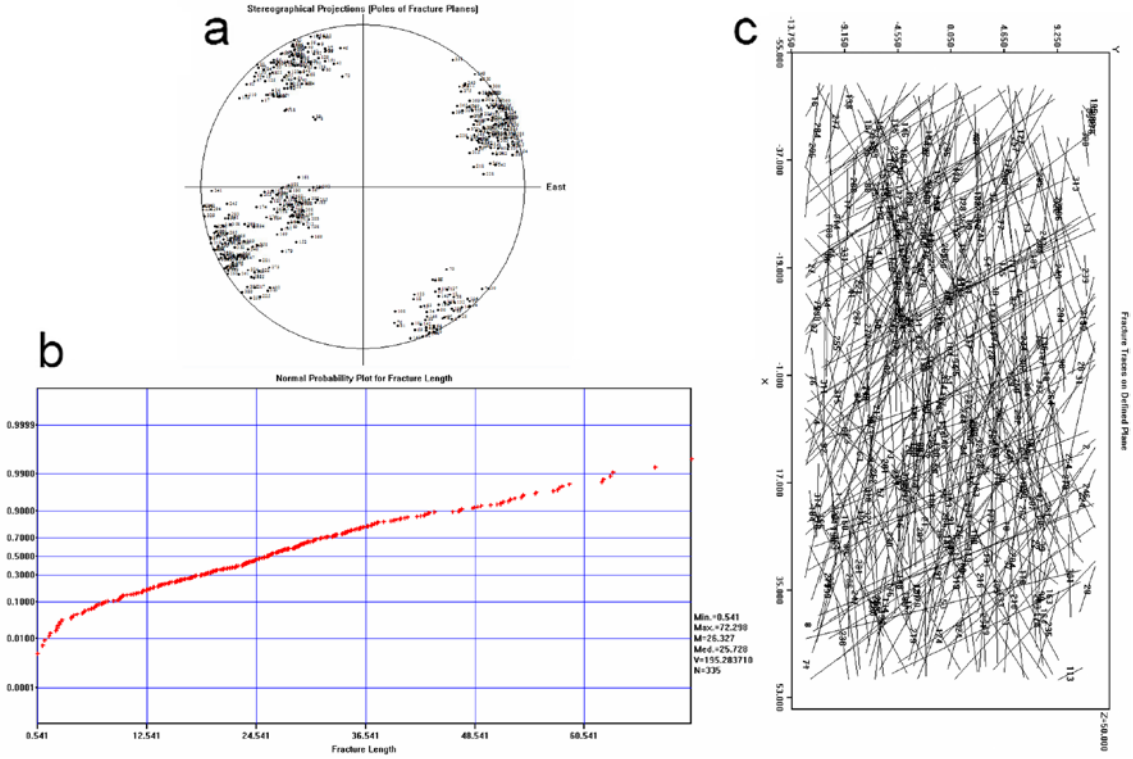

Figure 11. Generation of a DFN model for the marble buttress using FracSim3D FracSim3D with P_{10} certain+uncertain values. K1, K2 and K3 joint sets included. a) Stereonet, b) Normal probability plot for fracture lengths, c) 2D DFN model section.

6. Discussion

The adopted approach, based on the combined use of high-resolution UAV images and engineering geological data on a marble buttress, allowed the construction of a reliable 3D DFN rock mass model. Thanks to the acquisition of images from different angles it was possible to overcome data acquisition difficulties for high steep quarry walls and to create high-resolution orthophotos from different perspectives. GCPs measured using a Total Station and GPS receivers allowed for a high level of accuracy in the external orientation of photographs, which is particularly important for joint measurements. The methodology was used to obtain accurate deterministic measurements of discontinuity intensity and density for every joint set in the marble buttress. This was particularly important because the density and intensity of discontinuities can vary at different heights of the rock mass due to stress relaxation induced by excavation activity. An in-depth examination of the rock mass revealed differences in the discontinuities on different zones of the buttress. For example, the bottom of the buttress shows fewer discontinuities, probably because it has been excavated more recently and brittle fracturing associated with stress release has not yet propagated through the intact rock. The upper portions of the slope, instead, are more fractured. This difference is particularly evident in the S1 system (foliation): S1 discontinuities are numerous in the upper parts of the slope, whereas they are hard to find at the bottom of the buttress. In the lower buttress S1 is present only as a plane of weakness that may later evolve into a real discontinuity. This difference is also highlighted by P_{10}, P_{20} and P_{21} results.

Considering the buttress front, which is perpendicular to the supposed direction of relaxation of the structure, the density/intensity values of window 3 (upper window, 0.467) are substantially higher than those of window 4 (lower window, 0.133). Such information is very useful in creating reliable DFN models to be calibrated for stability analysis purposes. Therefore, the possibility to obtain information at different heights, could allow the generation of realistic DFN models achieved by creating subdomains where different P values can be used. Areas with high concentrations of S1 discontinuities are currently those most likely to experience problems due to stress relaxation and possibly failure. In future numerical modelling stability analyses it will be important to compare the obtained stress values with results from in-situ stress measurements (already planned in collaboration with the Massa and Carrara USL (Local Health Authority), Mining Engineering Operative Unit - Department of Prevention Hygiene Safety Workplace). This will allow better assessment of the possible effects of density/intensity values on DFN modelling and the stability of the buttress.

In addition, both certain and uncertain joint attitudes were discerned in this work. This was done because on a flat surface like a quarry wall face it is difficult to correctly interpret the set to which a discontinuity belongs, an important point requiring further studies in the context of DFN model calibration and validation. Although the geometric parameters required to build a DFN (fracture location, size, shape, orientation, density, flow property and number of sets) can all be derived deterministically through photointerpretation, additional statistical input is important for generating the discontinuity sets. The presence of joints with an uncertain attitude results in a model with a higher number of discontinuities showed by comparing figures 10 and 11. In fact, the DFN model obtained using $P_{certain+uncertain}$ values, resulted in a 32 % increase of the number of discontinuities, from 306 to 404 joints. On the other hand, uncertain discontinuities may not be representative of specific sets but of random fractures. The key aspect in this case is that the amount of data collected thanks to the adopted UAV-based approach can possibly lead to the development of a large number of different DFN models to be used for stability analysis purposes, which are more likely to satisfy the statistical criteria.

In this case study the particular shape of the buttress was an advantage: as the buttress was accessible from three sides, it was possible to create a complete 3D model of the rock mass. By measuring the joints from different perspectives, orientation bias was minimized. Moreover, it was possible to check whether the 3D DFN model obtained from the observation of 2D rock exposures was representative of the actual buttress condition. This is illustrated well by observing the obtained DFN stereonets (Figures 9, 10a and 11a) and the 2D DFN sections (Figures 9, 10c and 11c). Where, the results are very similar respectively to the engineering geological survey stereonet (Figure 3) and to the fracture traces observable on the deterministically mapped windows (Figures 7 and 8). In this regard, useful information can also be obtained by analysing fracture traces lengths. Francioni et al. (2015) reports that fracture trace lengths on the buttress range from 10 m to 30 m for K1, K2 and K3. This work correlates well with these findings, as illustrated in the two normal probability plots (figures 10b and 11b), which show that the majority of the fracture traces have lengths between 10 and 35 meters.

This validation of the model confirmed the quality of results and the great potential of UAV systems in detailed surveys, even in inaccessible areas. Conversely, possible limitations in the use of UAV can be linked to the need of a UAV pilot license and experience. In fact, the accuracy of the output, can be affected by quality of data collected (photos and GCPs), hardware and software availability and, last but not least, user experience. When performing manual photointerpretation, the precision and accuracy of measurements can vary, depending on the skill of the interpreter. Although several studies have demonstrated the use and reliability of automatic and semi-automatic processing of imagery and 3D point clouds for fracture mapping (Mah et al. 2011; Vöge et al. 2013; Assali et al. 2014; Vasuki et al. 2014), a fully manual approach was here adopted to guarantee consistency and quality in the interpretation of discontinuities. Note that in most cases the flat and regular morphology of quarry walls only allowed photointerpretation of discontinuity traces. Final visual inspection of outputs is always required, even when using codes for the semi-automatic extraction of joints.

7. Conclusions

One of the main advantages of using a UAV for rock slope stability studies is the ability to acquire data in inaccessible areas where foliation and fractures may vary their attitude and other fundamental geometric characteristics. Flight plans can be customized to reach any height above the ground so that observations are optimized and occlusions are avoided. UAV data collection is non-invasive, safe and inexpensive compared to TLS and helicopter surveys (no crew required). UAV surveys can be completed quickly. The produced DSM from 3D point clouds and orthophotos are easily interpreted and can be managed in a GIS environment. A large number of features can be accurately mapped both in 2D and 3D, with great flexibility in data editing.

This study shows how data from UAV image photointerpretation can be successfully used to study the geological structure of a rock mass and build a 3D DFN model of its fracture system. The importance of mapping uncertain joints has been highlighted, as well as the benefits of accurately measuring fracture density/intensity in different portions of the rock mass. Nevertheless, model calibration and validation using either in-situ stress measurement or displacement data are required to obtain reliable results.

Other advantages of using UAV systems in the study of rock slope stability are linked to the possible acquisition of multitemporal data, and the ability to update data and customize the nominal scale of photo shoots. The study of rock mass fracturing can greatly benefit from this type of approach in determining both yield (in terms of commercial value) and stability (in terms of safety). Within this context, GIS environments allow for the simple, comprehensive management, processing and analysis of georeferenced data.

Acknowledgments

Part of the present study was undertaken within the framework of the Italian National Research Project PRIN2009, funded by the Ministry of Education, Universities and Research, which involves the collaboration between the University of Siena, “La

Sapienza" University of Rome, and USL1 of Massa and Carrara (Mining Engineering Operative Unit – Department of Prevention). The authors acknowledge Pellegri, M. and Gullì, D. (USL1, Mining Engineering Operative Unit – Department of Prevention), Ferrari, M., Profeti, M. and Carnicelli, V. (Cooperativa Cavatori Lorano) and Chaoshui Xu (School of Civil, Environmental and Mining Engineering, University of Adelaide, South Australia) for their support of this research.

References

Abellán A, Vilaplana JM, Martinez J. 2006. Application of a long-range Terrestrial Laser Scanner to a detailed rock fall study at Vall de Núria (Eastern Pyrenees, Spain). Eng. Geol. 88:136-48.

Agisoft. 2016. Agisoft PhotoScan User Manual Professional Edition, Version 1.2.3.

Assali P, Grussenmeyer P, Villemin T, Pollet N, Viguier F. 2014. Surveying and modeling of rock discontinuities by terrestrial laser scanning and photogrammetry: Semi-automatic approaches for linear outcrop inspection. J. Struct. Geol. 66:102-114.

Bahrani N, Kaiser PK, Valley B. 2014. Distinct element method simulation of an analogue for a highly interlocked, non-persistently jointed rockmass. Int. J. Rock Mech. and Mining Sci. 71:117-130.

Bakun-Mazor D, Hatzor YH, Dershowitz WS. 2009. Modeling the mechanical layering effects on stability of underground openings in jointed sedimentary rocks. Int. J. Rock Mech. Min., 46:262-271.

Bieniawski ZT. 1989. Engineering Rock Mass Classifications. John Wiley and Sons, New York.

Boccaletti M, Elter P, Guazzone G. 1971. Plate tectonic models for the development of the Western Alps and Northern Apennines. Nature. 234:108-111.

Borghi A, Renard P, Fournier L, Negro F. 2015. Stochastic fracture generation accounting for the stratification orientation in a folded environment based on an implicit geological model. Eng. Geol. 187:135-142.

Carmignani L, Antompaoli L, Appelius V, Bocci M, Chiereghin F, Coli M, Fantozzi, PL, Frosini S, Grazioni B, Livi V, Mariottini E, Meccheri M, Piccini L, Pini G, Rossi LM, Sciuto PF. 2002. Studi conoscitivi sui bacini marmiferi industriali di Carrara: un contributo per la gestione pianificata dell'attività [Studies about industrial marble basins in Carrara: a contribute for the management of planning activity]. GEAM - Geoingegneria Ambientale e Mineraria. 24:21-43. In Italian.

Carmignani L, Conti P, Mancini S, Massa G, Meccheri M, Simoncini D, Vaselli L. 2007. Carta Giacimentologica dei Marmi delle Alpi Apuane - RELAZIONE FINALE [Map of the marble deposits of the Apuan Alps - Final Report]. Agreement Tuscany Region - University of Siena. In Italian.

Carmignani L, Kligfield R. 1990. Crustal extension in the northern Apennines: the transition from compression to extension in the Alpi Apuane Core Complex. Tectonics 9:1275-1303.

Coggan JS, Wetherelt A, Gwynn XP, Flynn Z. 2007. Comparison of hand-mapping with remote data capture systems for effective rock mass characterisation. In: Ribeiro e Sousa L, Olalla C, Grossmann N, editors. The second half century of rock mechanics. Proceedings of the 11th Congress of the Internation Society of Rock Mechanics; 2007 July 9-13; Lisbon. 1:201-205.

Danzi M, Di Crescenzo G, Ramondini M, Santo A. 2013. Use of unmanned aerial vehicles (UAVs) for photogrammetric surveys in rockfall instability studies. Rendiconti Online Soc. Geol. It. 24:82-85.

Dercourt J, Zonenshain LP, Ricou LE, Kazmin VG, Le Pichon X, Knipper AL, Grandjacquet C, Sbortshikov IM, Geyssant J, Lepvrier C, Pechersky DH, Boulin J, Sibuet JC, Savostin LA, Sorokhtin O, Westphal M, Bazhenov ML, Lauer JP, Biju-Duval B. 1986. Geological evolution of the Tethys belt from the Atlantic to the Pamirs since the Lias. Tectonophysics 123:241-315.

Dershowitz WS, Einstein HH. 1988. Characterizing rock joint geometry with joint system models. Rock Mech. Rock Eng. 21:21-51.

Dershowitz WS, Herda H. 1992. Interpretation of fracture spacing and intensity. In: Balkema AA editor. Proceedings of the 33rd U.S. Symposium on Rock Mechanics (USRMS); 3-5 June; Santa Fe (New Mexico).

Elter P. 1975. L'ensemble ligure [The Ligure complex]. Bull. Soc. Geol. France. 17:984-997. In French.

Ferrero AM, Forlani G, Rondella R, Voyat HI. 2009. Advanced geostructural survey methods applied to rock mass characterization. Rock Mech. Rock Eng. 42:631-65.

Francioni M, Salvini R, Stead D, Giovannini R, Riccucci S, Vanneschi C, Gullì D. 2015. An integrated remote sensing-GIS approach for the analysis of an open pit in the Carrara marble district, Italy: Slope stability assessment through kinematic and numerical methods. Comput. Geotech. 67:46-63.

Ghirotti M, Genevois R. 2007. A complex rock slope failure investigated by means of numerical modelling based on laser scanner technique. In: Eberhardt E, Stead D, Morrison T, editors. Proceedings of the 1st Canada-US Rock Mechanics Symposium; 2007 May 27-31; Vancouver (CA), p. 917-924.

Giordan D, Manconi A, Facello A, Baldo M, Dell'Anese F, Allasia P, Dutto F. 2015. Brief Communication: The use of an unmanned aerial vehicle in a rockfall emergency scenario. Nat. Hazards Earth Syst. Sci. 15:163-169.

Grenon M, Bruneau G, Kapinga Kalala I. 2014. Quantifying the impact of small variations in fracture geometric characteristics on peak rock mass properties at a mining project using a coupled DFN-DEM approach. Comput. Geotech. 58:47-55.

Hoek E, Brown ET. 1997. Practical estimates of rock mass strength. Int. J. Rock Mech. Min. Sci. 34:1165-1186.

569 Jaboyedoff M, Oppikofer T, Abellàn A, Derron MH, Loye A, Metzger R, Pedrazzini A,
570 2012. Use of LIDAR in landslide investigations: a review. Nat. Hazards. 61:5-28.

571 Lato M, Diederichs MS, Hutchinson DJ, Harrap R. 2009. Optimization of LiDAR
572 scanning and processing for automated structural evaluation of discontinuities in
573 rock masses. Int. J. Rock Mech. Min. Sci. 46:194-199.

574 Lei Q, Latham JP, Xiang J, Tsang CF, Lang P, Guo L. 2014. Effects of geomechanical
575 changes on the validity of a discrete fracture network representation of a realistic
576 two-dimensional fractured rock. Int. J. Rock Mech. Min. Sci. 70:507-523.

577 Lorig LJ. 2014. Application of discrete fracture networks in mining and civil
578 engineering. Paper presented at: DFNE 2014, 1st Int. Conf. Discrete Fracture
579 Network Eng., Vancouver, British Columbia, Canada.

580 Mah J, Samson C, McKinnon S. 2011. 3D laser imaging for joint orientation analysis.
581 Int. J. Rock Mech. Min. Sci. 48:932-941.

582 Meccheri M. 1996. Carta Geologico - Strutturale delle varietà merceologiche dei Marmi
583 del Carrarese Scala 1:10,000 [Structural-Geological map of the of the Marble
584 varieties in the Carrara area. Scale 1:10,000]. University of Siena, Department of
585 Earth Sciences. In Italian.

586 Molli G, 2008. Northern Appennine-Corsica orogenic system: an updated review. J.
587 Geol. Soc. London Special Publication. 298:413-442.

588 Molli G. 2012. Deformation and fluid flow during underplating and exhumation of the
589 Adria Continental margin: A one-day field trip in the Alpi Apuane (northern
590 Apennines, Italy). GSA Field Giudes. 28:35-48.

591 Molli G, Cortecci G, Vaselli L, Ottria G, Cortopassi A, Dinelli E, Mussi M, Barbieri M.
592 2010. Fault zone structure and fluid-rock interaction of a high angle normal fault
593 in Carrara marble (NW Tuscany, Italy). J. Struct. Geol. 32:1334-1348.

594 Molli G, Meccheri M, 2000. Geometrie di deformazione nell'alta valle di Colonnata: un
595 esempio di deformazione polifasica e composita nelle Alpi Apuane [Deformed
596 geometries in the Colonnata high valley: an example of complex poly-phased
597 deformation on the Apuan Alps]. Bull. Soc. Geol. It. 119:379-394. In Italian.

598 Molli G, Meccheri M, 2012. Structural inheritance and style of reactivation at mid-
599 crustal levels: A case study from the Alpi Apuane (Tuscany, Italy).
600 Tectonophysics. 579:74-87.

601 Niethammer U, James MR, Rothmund S, Travelletti J, Joswig M. 2012. UAV-based
602 remote sensing of the Super-Sauze landslide: Evaluation and results. Eng. Geol.
603 128:2-11.

604 Profeti M, Cella R, 2010. Relazione sulla stabilità dei fronti [Technical report about
605 stability analysis of rock faces]. Cooperativa Cavatori Lorano. In Italian.

606 Rau JY, Jhan JP, Lo CF, Lin YS. 2011. Landslide Mapping Using Imagery Acquired by
607 a Fixed-Wing UAV. In: Eisenbeiss H, Kunz M, Ingensand H, editors.
608 International Archives of the Photogrammetry, Remote Sensing and Spatial
609 Information Sciences. Proceedings of the International Conference on Unmanned

610 Aerial Vehicle in Geomatics (UAV-g); 2011 September 14-16; Zurich.
611 Switzerland.

612 Salvini R, Francioni M, Fantozzi PL, Riccucci S, Bonciani F, Mancini S. 2011. Stability
613 analysis of “Grotta delle Felci” Cliff (Capri Island, Italy): structural, engineering-
614 geological, photogrammetric surveys and laser scanning. Bull. Eng. Geol.
615 Environ. 70:549-557.

616 Salvini R, Francioni M, Riccucci S, Bonciani F, Callegari I. 2013. Photogrammetry and
617 laser scanning for analyzing slope stability and rock fall runout along the
618 Domodossola-Iselle railway, the Italian Alps. Geomorphology. 185:110-122.

619 Salvini R, Riccucci S, Gullì D, Giovannini R, Vanneschi C, Francioni M. 2014.
620 Engineering Geology for Society and Territory - Vol. 5 Urban Geology,
621 Sustainable Planning and Landscape Exploitation. Chapter 188, Geological
622 Application of UAV Photogrammetry and Terrestrial Laser Scanning in Marble
623 Quarrying (Apuan Alps, Italy); p. 979-984.

624 Salvini R, Vanneschi C, Riccucci S, Francioni M, Gullì D. 2015. Application of an
625 integrated geotechnical and topographic monitoring system in the Lorano marble
626 quarry (Apuan Alps, Italy). Geomorphology. 241:209-223.

627 Scandone P, 1979. Origin of the Tyrrhenian Sea and Calabrian Arc. Boll. Soc. Geol. It.
628 98:27-34.

629 Scholtès L, Donzé FD. 2012. Modelling progressive failure in fractured rock masses
630 using a 3D discrete element method. Int. J. Rock Mech. Min. Sci. 52:18-30.

631 Sturzenegger M, Stead D. 2009(a). Close-range terrestrial digital photogrammetry and
632 terrestrial laser scanning for discontinuity characterization on rock cuts. Eng.
633 Geol. 106:163-182.

634 Sturzenegger M, Stead D. 2009(b). Quantifying discontinuity orientation and
635 persistence on high mountain rock slopes and large landslides using terrestrial
636 remote sensing techniques. Nat. Haz. Earth Syst. Sci. 9:267-287.

637 Turner D, Lucieer A, De Jong SM. 2015. Time series analysis of landslide dynamics
638 using an unmanned aerial vehicle (UAV). Remote Sensing 7:1736-1757.

639 Vasuki Y, Holden EJ, Kovesi P, Micklethwaite S. 2014. Semi-automatic mapping of
640 geological structures using UAV-based photogrammetric data: an image analysis
641 approach. Comput. Geosci. 69:22-32.

642 Vöge M, Lato MJ, Diederichs MS. 2013. Automated rockmass discontinuity mapping
643 from 3-dimensional surface data. Eng. Geol. 164:155-162.

644 Weir FM, Fowler M. 2014. Application of DFN modelling to large open pit slope
645 design in Australia. Paper presented at: DFNE 2014, 1st Int. Conf. Discrete
646 Fracture Network Eng., Vancouver, British Columbia, Canada.

647 Xu C, Dowd P. 2010. A new computer code for discrete fracture network modelling.
648 Comput. Geosci. 36:292-301.

649 Zaccagna D. 1932. Descrizione Geologica delle Alpi Apuane [Geological description of
650 the Apuan Alps]. Memorie Descrittive della Carta Geologica d'Italia. 25:1-440. In
651 Italian.